JOM Journal of Optical Microsystems

RESEARCH PAPER

Programmable phase change materials and silicon photonics co-integration for photonic memory applications: a systematic study

Amin Shafiee,[a] Benoit Charbonnier,[b] Jie Yao,[c] Sudeep Pasricha,[a] and Mahdi Nikdast[a,*]

[a]Colorado State University, Department of Electrical and Computer Engineering, Fort Collins, Colorado, United States

[b]Université Grenoble Alpes, CEA-Leti, Grenoble, France

[c]University of California, Berkeley, Department of Materials Science and Engineering, Berkeley, California, United States

ABSTRACT. The integration of phase change materials (PCMs) with photonic devices creates a unique opportunity for realizing application-specific, reconfigurable, and energy-efficient photonic components with zero static power consumption and low thermal crosstalk. In particular, photonic waveguides based on silicon or silicon nitride can be integrated with PCMs to realize nonvolatile photonic memory cells, which are able to store data in the phase state of the PCMs. We delve into the performance comparison of PCM-based programmable photonic memory cells based on silicon photonic and silicon nitride platforms using known PCMs (GST and GSST) for photonic memory applications while showcasing the fundamental limitations related to each design in terms of the maximum number of bits that they can store as well as their optical insertion loss. Moreover, we present comprehensive design-space exploration for analyzing the energy efficiency and cooling time of the photonic memory cells depending on the structure of the heat source. The results show that the silicon-based strip waveguide integrated with GST is the best option to realize a photonic memory cell with the highest bit density (up to 4-bits per cell given 6% spacing between the optical transmission levels). In addition, considering a microheater integration on top of a waveguide on which PCM is deposited, multi-physics simulation results show that as the heat source is placed above the PCM with a gap of 200 nm, the photonic memory cell tends to become more energy-efficient, and the cooling time of the PCM (for set and reset) becomes significantly shorter than the case where the heat source is placed further from the PCM.

Keywords: phase change materials; silicon photonics; photonic memory; photonic computing systems

Paper 24006SS received Mar. 1, 2024; revised Jul. 10, 2024; accepted Jul. 24, 2024; published Aug. 14, 2024.

1 Introduction

In the post-Moore era, conventional CMOS-based integrated circuits are struggling to meet the performance requirements related to emerging data-driven applications, which include large language models, intrusion detection systems, and pandemic growth detection systems. In particular, conventional electronic memory technologies, such as DRAMs and SRAMs, are facing constraints due to manufacturing scalability concerns, data retention problems, power penalties,

*Address all correspondence to Mahdi Nikdast, Mahdi.Nikdast@colostate.edu

leakage issues, and bandwidth limitations.[1–3] Nonvolatile memories (NVMs) based on ferroelectric materials, such as FeRAMs, and resistive metal oxides, such as ReRAMs, can address the data retention issues related to DRAMs and SRAMs. Despite the promise of NVMs, they suffer from reliability issues and limited write endurance. This motivates the need for a new alternative NVM for emerging communication and computation systems.

NVMs based on phase change materials (PCMs) can offer superior bit density, energy efficiency, reliability, and bandwidth.[4–8] PCMs are a class of chalcogenides that can repeatedly change their state from amorphous to crystalline, and vice versa, in a nonvolatile manner when exposed to an external heat source. The phase changes result in some changes in the optical and electrical properties of the material in different states. This unique property makes PCMs a suitable candidate to implement reconfigurable photonic devices as they experience changes in their optical characteristics with phase state changes. When a PCM is heated, the absorbed energy from the heat source changes the temperature of the material. When the temperature of the PCM is higher than its glass temperature and lower than its melting temperature (e.g., glass temperature for GST is 453 K and the melting temperature is 890 K[9,10]), the crystallization of the material is triggered. When the energy of the heat source is high enough to increase the temperature of the material to values higher than the melting temperature, due to the melt and quenched procedure, the PCM can be considered to have an amorphous state. Note that the phase state of the PCMs is nonvolatile, meaning that in the absence of an external heat source, the material tends to maintain its phase state. The nonvolatile phase transition of PCMs can be leveraged to implement NVM cells where we can store data using the state of the material.[11–15]

A single nonvolatile PCM-based photonic memory cell can be implemented by depositing a thin layer of PCM on silicon or silicon nitride waveguides. When the PCM on top of the waveguide has an amorphous state, because of light-matter interactions between the propagating mode and the PCM, a portion of the input light will be absorbed by the PCM, leading to some attenuation in the optical transmission (i.e., the amount of optical power received at the output) at the output of the waveguide. When the PCM is heated to a temperature above the glass temperature and lower than the melting temperature, the crystallization process starts. This results in the change in the PCM's optical properties, which leads to higher optical losses (i.e., the amount of optical power absorbed in PCM due to light-material interaction) and lower optical transmission at the output of the PCM-loaded waveguide, compared to the case where the PCM is in the amorphous state. Therefore, by controlling the amount of energy provided by the heat source, one can control the crystallization fraction the portion of the volume, which is in the crystalline state within the PCM (X_f) of the PCM, hence achieving multiple distinctive optical transmission levels at the output. The distinctive optical transmission levels that are a function of the PCM's state can be used to store data in the optical domain (see Fig. 1).[14,16–20]

Despite the great promise of PCMs for implementing reconfigurable photonic devices, such as photonic memories, they suffer from a few limitations. For example, PCM-based photonic devices are susceptible to optical loss due to scattering and back-reflection of light at the PCM-waveguide interface[17] due to the drastic contrast between the optical properties of PCMs and the waveguide material. Although research on PCM-based reconfigurable photonic devices is still in progress, it mostly focuses on the experimental characterization of PCM-based photonic memory cells with a fixed geometry. The novel contribution of this paper is to present a comprehensive and systematic design-space exploration framework that can take experimental characterizations as an input to co-design PCM-based photonic memory cells (see Fig. 2) and analyze their optical insertion loss, transmission variation due to light scattering and back-reflections, and the maximum bit capacity per cell. The presented framework is valuable as it paves the way for analyzing the behavior of the PCM-based photonic memory cell before the fabrication and characterization of the devices. Moreover, we also perform a design-space exploration for the heater design for photonic memory cells to characterize the required energy for the phase transition in PCM-based photonic memories, to explore the most energy-efficient solutions.

2 Background and Related Prior Work

In this section, we first present an overview of the optical properties of some known PCMs for photonic memory applications: Sb_2S_3, Sb_2Se_3, GST ($Ge_2Sb_2Te_5$), and GSST ($Ge_2Sb_2Se_4Te$).

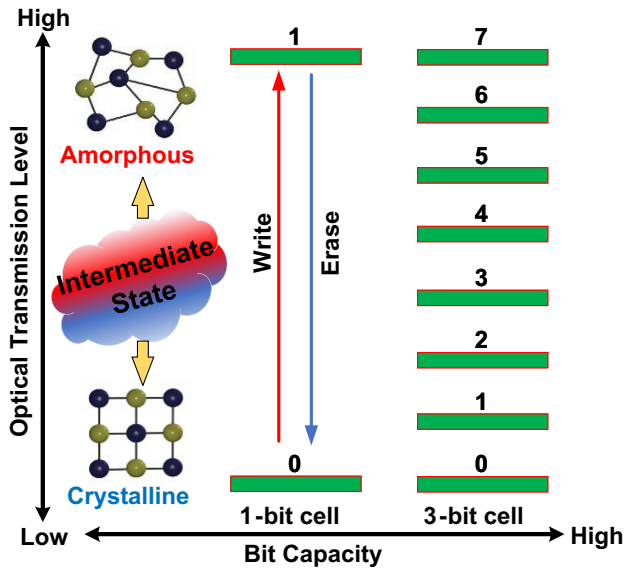

Fig. 1 Schematic of PCM-based photonic memory cell's working principle. Distinctive phase states lead to distinctive optical transmission levels, which can be used to store multiple bits per PCM cells.[14]

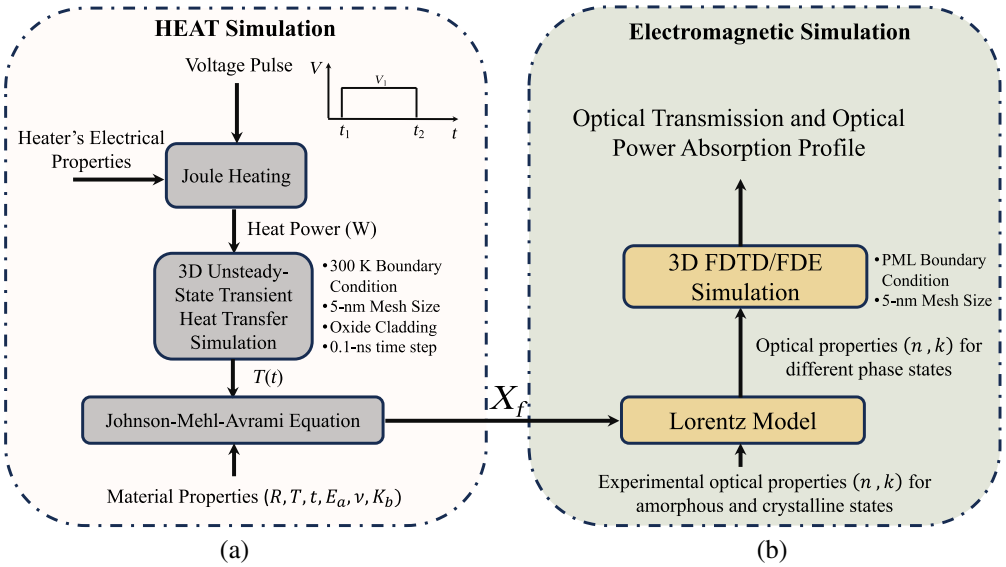

Fig. 2 Framework of the simulations presented in this work for PCM-based reconfigurable photonic devices. (a) The simulation steps to perform the unsteady-state and transient heat transfer simulation to capture the temperature distribution as a function of time $(T(t))$ to capture the crystallization fraction (X_f) according to the JMA equation. Note that one can replace the JMA equation with classical nucleation theory.[21] In addition, as the metallic heaters are used as a heat source in this paper, the voltage pulse can be converted to heat power through Joule's heating. (b) The steps for electromagnetic simulations for PCM-based reconfigurable devices based on the crystallization fraction value of the PCM in the device to capture the optical transmission levels and optical power absorption levels as a function of X_f.

Then, we provide an overview of some recent prior work on the integration of PCMs with photonic platforms to realize photonic memories. We also define the performance metrics for the design, optimization, and performance comparison of PCM-based photonic memory cells to choose the suitable candidates to implement PCM-based photonic memory cells.

2.1 Optical and Thermal Properties of PCMs

A PCM's phase state can change from amorphous to crystalline state, and vice versa, when the material absorbs energy from an external heat source. Depending on the phase state of PCMs, their optical and thermal characteristics change. An important parameter for modeling the optical properties of PCMs in any arbitrary state is the crystallization fraction (X_f), which determines the portion of the material's volume that is in the crystalline state. The crystallization fraction can take a number between 0 and 1 where 0 represents a fully amorphous state and 1 represents a fully crystalline state.[22] As the crystallization fraction increases from 0 to 1, the complex refractive index of the PCM, which can be defined as $n^c = n + i\kappa$, increases. To model the complex refractive index of PCMs in any arbitrary state between the fully crystalline and fully amorphous states as a function of the crystallization fraction, the Lorentz model can be used, as shown below:

$$\frac{\varepsilon_i(\lambda)-1}{\varepsilon_i(\lambda)+2} = (X_f)\frac{\varepsilon_c(\lambda)-1}{\varepsilon_c(\lambda)+2} + (1-X_f)\frac{\varepsilon_a(\lambda)-1}{\varepsilon_a(\lambda)+2}, \tag{1}$$

$$\varepsilon_{a,c,i} = n_{a,c,i}^2. \tag{2}$$

In Eq. (1), X_f is the crystallization fraction value; λ is the operating wavelength; ε_a and ε_c are, respectively, the complex permittivity of the PCM in the amorphous and crystalline states; and ε_i is the permittivity of the PCM at any arbitrary state as a function of X_f. Note that the complex refractive index ($n^c = n + i\kappa$) profile of PCMs can be calculated using the complex permittivity according to Eq. (2). The optical properties of some of the known PCMs C-band are shown in Fig. 3. As was mentioned, the PCM-based photonic memories are introduced as an alternative to CMOS-based NVMs to be used in high performance computing systems to eliminate the need for the power hungry electro-optical and opto-electrical conversions. Most of the high-performance photonic computing systems operate at the C-band operating wavelength range. This motivates choosing C-band (1500 to 1600 nm) for this work.[14,25–28] Observe that in all of the case studies, as the phase state of the PCM shifts to the crystalline state, the extinction coefficient (κ) increases, which results in increased light absorption by the material. When integrated with a photonic waveguide, this unique property of PCMs leads to multiple transmission levels as the phase state of the PCM is changed from amorphous to crystalline or a hybrid state where some portion of the material is in the crystalline state and the rest of the material is in the amorphous state. As the crystallization fraction increases, the light absorption increases and this leads to decreased optical transmission. Therefore, we can leverage these multiple transmission levels for PCMs integrated with photonic waveguides to realize a single photonic memory cell where it is possible to store data as part of the state of the material in a nonvolatile manner.

In addition, the thermal properties of PCMs change as the phase transition is triggered. The thermal properties of the PCMs in crystalline and amorphous states considered in this work are reported in Table 1. We can see that the thermal properties, such as thermal conductivity, heat capacity, and density, change as the phase state of the PCM changes, and this will affect the heat transfer kinetics through the PCM, such as the crystallization and amorphization of the PCM.[9,11] Note that in general, the thermal properties of the PCMs do not change linearly over the full temperature cycle where the phase state of the material changes. However, in the simulations presented in this work, we assumed that thermal properties are constant when heating the material and change linearly when the phase state of the PCM changes from amorphous to

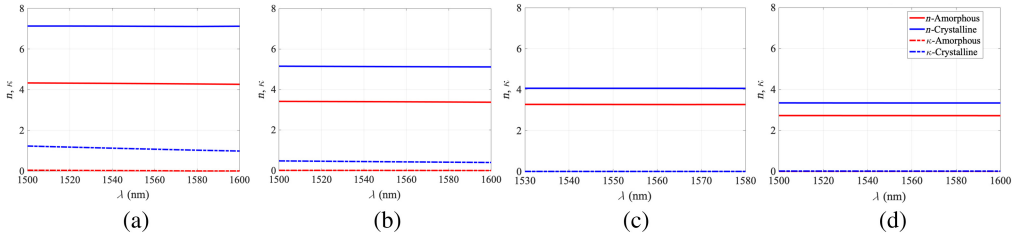

Fig. 3 Wavelength dependent optical refractive index (n) and extinction coefficient (κ) for different PCM materials and wavelengths.[23,24] (a) GST's optical refractive index profile, (b) GSST's optical refractive index profile, (c) Sb_2Se_3's optical refractive index profile, and (d) Sb_2S_3's optical refractive index profile.

Table 1 Thermal properties of popular PCMs (a: amorphous and c: crystalline).

Material	Thermal conductivity (W/mK)	Heat capacity (C_p; J/gK)	Density (ρ; g/cm^3)
a-GST[27,29,30]	0.19	0.213	5.87
c-GST[27,29,30]	0.57	0.199	6.27
a-GSST[27,29]	0.2 ± 0.02	1.5 ± 0.1	5.27
c-GSST[27,29]	0.48 ± 0.06	1.8 ± 0.1	5.53

crystalline states and vice versa.[21,28,29,31,32] Note that this is a valid assumption due to the thin PCM cells (with thickness values <100 nm) considered in this paper. The same assumption is considered by Wang et al.[21] where it has been validated through experimental tests.

2.2 Crystallization Kinetics in PCMs

The crystallization kinetics of the PCMs in the case of isothermal heating is governed by the growth process[32–34] and can be modeled based on two models of classical nucleation theory and Johnson–Mehl–Avrami (JMA) theory.[21] In this paper, the JMA theory is used to predict the volume of the PCM transformed to crystalline state after the isothermal duration of t utilizing the well-known JMA:[32,33,35]

$$X_f = 1 - \exp(-(Rt)^m), \tag{3}$$

where X_f is the PCM's crystallization fraction after the time t, R is the crystallization rate, and m is Avrami constant. The crystallization of the PCMs occurs for temperature values well below the melting temperature[9] governed by the diffusion-limited regime. Therefore, the crystallization rate R can be characterized by the Arrhenius equation based on Eq. (4):

$$R(T) = \nu \exp\left(\frac{-E_a}{K_b T}\right). \tag{4}$$

In Eq. (4), E_a stands for the PCM's crystallization activation energy,[33,35,36] ν stands for PCM's frequency factor, K_b is the Boltzmann constant, and T is the temperature of the PCM. Note that doping the PCMs leads to change in the Avrami constant values compared to intrinsic PCMs, which can results in a more gradual crystallization. Therefore, a higher number of stable crystallization levels in the presence of temperature variations can be achieved.

2.3 Figure of Merit

PCMs can be used in a variety of applications for reconfigurable photonics from phase shifters and optical multipliers[12,17,37,38] to photonic memory cells.[4] To choose a suitable material for each specific application, a figure of merit (FOM) should be defined. For memory applications, high absorption in the crystalline state and low absorption in the amorphous state are desired to take advantage of optical transmission contrast stemming from the optical absorption contrast to store the data.[20] The absorption coefficient of the PCM can be analytically calculated according to

$$\alpha = \frac{4\pi\kappa}{\lambda}. \tag{5}$$

In this equation, α is the absorption coefficient per unit length (cm^{-1}), κ is the extinction coefficient, and λ is the operating wavelength. Observe that for a fixed wavelength, as κ increases, the material's absorption per unit length also increases. Moreover, for PCM-based photonic memory applications, low refractive index contrast (Δn) between the amorphous and crystalline state is preferred. The reason for this is that as the refractive index contrast between the amorphous and crystalline states increases, the propagating light in the waveguide may encounter a more severe scattering effect when interacting with the PCM, which can lead to an uncontrolled transmission change at the output of the waveguide.[20,32]

Accordingly, Δ_κ/Δ_n can be used as an FOM to select a suitable material for implementing PCM-based photonic memories. As the FOM increases, the material experiences higher

absorption contrast between crystalline and amorphous states and lower refractive index contrast between the two states above. From Fig. 3, compared to Sb_2S_3 and Sb_2Se_3, only GST and GSST result in nonzero FOM, making them preferred candidates for photonic memory applications. Moreover, at the 1550 nm wavelength point, the FOM for GST is 0.38 and it is 0.24 for GSST, making GST a better candidate for photonic memory applications. Therefore, these two materials are considered to implement photonic memory cells in the rest of this paper. Note that the low absorption and high refractive-index contrast of Sb_2Se_3 and Sb_2S_3 make them a good candidate for PCM-based phase shifter applications, such as in photonic switching networks, photonic computation units, and optical communication systems.[12,17,37,39–42]

2.4 Related Prior Work

In this section, we present an overview of related prior work on PCM-based photonic memories. One of the very first efforts presented a PCM-based photonic memory cell by integrating a 5-μm long GST with 10 nm thickness with a silicon nitride ridge waveguide.[14] Rios et al.[14] showed that by changing the phase state of the GST from amorphous to crystalline state by exposing it to an intense laser pulse with energy of 533 pJ, the readout of the cell changes by about 21%, as about 80.7% of the input light was absorbed in the PCM. Hence demonstrating the promise of realizing a photonic memory cell using PCMs to store a single logic bit.

Li et al.[10] presented a programming scheme to enable a 5-bit PCM-based photonic memory, realizing 34 distinctive optical transmission levels. In particular, they showed that their programming scheme is independent of the previous phase state of the PCM. However, the authors did not present any system-level results when applying their multi-step programming scheme to trigger the phase transition of the PCM. Moreover, the margins among the optical transmission levels in Li et al.[10] were considered to be about 1%. Such a narrow margin makes the design impractical to be used in optical communication and computation systems due to the transmission drifts in the PCM cells over time as well as the required voltage precision in the optical receiver to convert the narrowly spaced optical transmission levels to electrical signals.[4,20,43,44]

An addressing scheme using wavelength-division multiplexing and PCMs was presented by Feldmann et al.[18] Non-volatile storage is created by integrating PCMs with microring resonators to realize a data storage element, thus removing the need to continuously refresh the memory. The authors showed that by cascading silicon nitride-based microring resonators integrated with PCMs, a memory array can be realized that is able to store up to 512-bit data in total.

Youngblood et al.[28] presented a time-dependent, multiphysics simulation framework to leverage experimental results, allowing to capture recrystallization dynamics and their fraction within memory cells. As a result, this unique approach to photonic memory facilitates both data storage with tunable volatility and the detection of coincident events between two pulse trains. They showed that using their simulation scheme, one can predict the crystallization fraction of the PCM given the amount of energy that is provided to PCM.

More recently, Xia et al.[25] showed that for a fixed geometry of the waveguide integrated with GST, doping the GST with nitrogen dopants (N-GST) leads to an increased glass temperature of the PCM. This results in grain growth of GST when crystallization occurs, giving a more progressive crystallization process with the grain-refinement phenomenon. This leads to higher number of modulation states defined by stable intermediate states, and in turn results in having higher number of stable optical transmission levels making the PCM cell capable of storing more than 7 bits per cell. However, Xia et al.[25] neglect the system-level requirements related to minimum spacing between the transmission levels, so the optical receiver in the system can translate the optical transmission level to an electrical signal. An indium tin oxide (ITO) heater controlled by a voltage source was used in this work to provide the required heat to trigger the phase change of N-GST. The summary of some of the prior works on experimental implementation and characterization of PCM-based photonic memory cells is reported in Table 2.

Previous research has primarily concentrated on the experimental realization and characterization of PCM-based photonic memory cells with fixed geometries, often neglecting the limitations at the material and device levels and the importance of performance prediction prior to fabrication. In contrast, this paper provides a thorough exploration of the design space for PCM-based photonic memory cells, from the material level to the device level, utilizing multiphysics simulations. The simulation results are then employed to elucidate the fundamental

Table 2 Summary of the prior work on photonic memory cells discussed in this paper.

Ref.	PCM	Waveguide	Switching	# Levels	Cell structure
14	GST	Si_3N_4	Optical	2	MRR/ridge waveguide
10	GST	Si_3N_4	Optical	32	Ridge waveguide
28	GST	Si_3N_4	Optical	9	MRR
25	N-GST	Silicon	ITO heater	222	Ridge waveguide
4	GST	Silicon	Ti/TiN metallic heater	16	MRR
8	GST	Si_3N_4	Optical	32	Ridge waveguide
9	GST	Silicon	Ti/Pt metallic heater	—	Ridge waveguide
21	GST	Si_3N_4	Optical	12	Strip waveguide
45	GSSe	Silicon	W/Ti metallic heater	15	Ridge waveguide
27	GST	Si_3N_4/silicon	Optical	6	Ridge waveguide
46	GST	Si_3N_4/silicon	Optical	32	Waveguide crossing
47	GSST	Silicon	Doped Si heater	18	Ridge waveguide

limitations of PCM-based photonic memory cells, including bit density, insertion loss, optical transmission deviations due to light scattering, and energy efficiency when metallic heaters are used for phase transitions in the PCM.

3 PCM-Based Photonic Memory Cells

PCM-based photonic memory cells can be fabricated by depositing PCM on top of a conventional waveguide, such as silicon or silicon nitride strip or ridge waveguide as shown in Fig. 4.[17,22,25] In this section, we first present a comprehensive design-space exploration of cell insertion loss and bit capacity for the four case studies shown in Fig. 4 according to the framework depicted in the right-hand side of Fig. 2. Then, we perform a design-space exploration and performance comparison in terms of energy efficiency and cooling time to implement a metallic-based microheater to provide sufficient energy for PCMs to trigger their phase transition based on the left-hand side framework shown in Fig. 2.

3.1 Optical Insertion Loss in PCM-Based Photonic Memory Cells

As the PCM starts to crystallize, the optical refractive index profile of the deposited PCM will change, impacting the optical transmission level at the output of the waveguide. Optical loss in PCM-based reconfigurable photonic devices depends on the target application. For example, for photonic switches using PCMs, an optical loss in both phase states of amorphous and crystalline is preferred. For photonic memory applications, the optical loss stemming from the absorption of the light in the PCM is favorable to encode the data on the distinctive optical transmission levels.[20] In PCM-based photonic memory cells, the maximum optical transmission is required

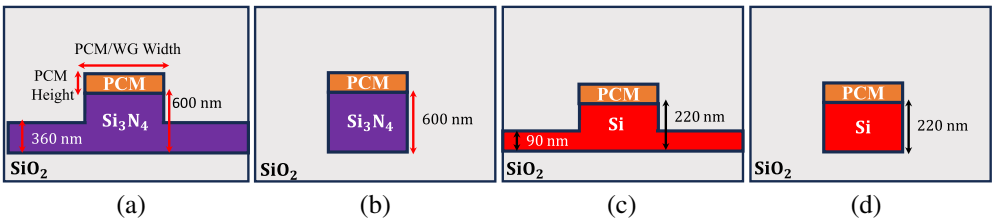

Fig. 4 Schematic of PCM-based photonic memory cells considered in this work based on CEA-leti standard foundry. (a) Silicon nitride-based ridge waveguide, (b) silicon nitride-based strip waveguide, (c) silicon-based ridge waveguide, and (d) silicon-based strip waveguide. For all of the cases, the oxide cladding has been considered.

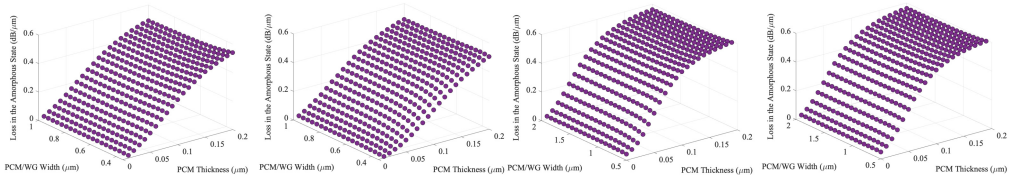

Fig. 5 GST-based photonic memory cell's optical insertion loss for the geometries reported in Fig. 4 at 1.55 μm operating wavelength. Note that the optical loss for GSST, Sb_2S_3, and Sb_2Se_3 will be negligible due to their negligible absorption in both crystalline and amorphous state, hence, they are not reported. (a) GST-loaded silicon strip waveguide, (b) GST-loaded silicon ridge waveguide, (c) GST-loaded silicon nitride ridge waveguide, and (d) GST-loaded silicon nitride strip waveguide.

when the PCM is in the amorphous state and negligible optical transmission is desired when the PCM is in the crystalline state. Hence, the optical transmission when the PCM is in the amorphous state can be used to calculate the insertion loss of the cell in the amorphous state.

The optical insertion loss in the amorphous state per unit length (dB/μm) for the four case studies in Fig. 4 is shown in Fig. 5. Note that the results for GSST are not reported here due to the zero loss at the amorphous state (see Fig. 3(b)). Observe that the optical insertion loss for the silicon waveguide is slightly lower than the silicon nitride waveguide, especially for low values of PCM thickness due to smaller refractive index contrast between the PCM and silicon at 1550 nm ($n_{Si} = 3.48$ and $n_{GST} = 4.15$). Moreover, the insertion loss for the silicon ridge waveguide is slightly lower than the strip waveguide. The effective refractive index for the ridge waveguides is higher than for the strip waveguides. This can be physically interpreted as higher confinement of optical mode in ridge waveguides compared to strip waveguides. Therefore, the optical signal interacts less with the PCM when ridge waveguides are used to implement PCM-based photonic memory cell. This results in a lower insertion loss when the PCM in the amorphous state. This is more visible for thin film PCMs. Note that the results reported in Fig. 5 are consistent with the optical insertion loss reported by Xia et al.[25] where they report 0.2107 dB/μm optical insertion loss in the amorphous state for a 20 nm thick GST on top of silicon ridge waveguide.

3.2 Bit Density and Scattering Effect in PCM-Based Photonic Memory Cells

The phase state of PCMs can be used to store data when implementing PCM-based photonic memories. As the PCM's crystallization fraction increases, the optical transmission decreases because of the increased absorption in the material. The multiple optical transmission levels as a function of crystallization fraction can be used to store multiple bits on the state of the PCM. For example, to store 2 bits per PCM cell, the PCM on top of the waveguide should provide four distinctive transmission levels to store "00," "01," "10," and "11" in the memory cell. Therefore, as the optical transmission contrast between the two specific states of fully amorphous and fully crystalline increases, the number of distinctive optical transmission levels increases, hence, the bit density per cell increases. However, the optical transmission contrast between the amorphous and crystalline states itself is not an adequate parameter for calculating the bit density per cell. In the previous section, we explained that the optical refractive index contrast between the PCMs and the waveguide material can be extremely high, especially when the PCM is in the crystalline state. This leads to pulling the optical mode toward the PCM because of its higher refractive index compared to silicon or silicon nitride when propagating in the waveguide. This results in the scattering of light and its back-reflection at the PCM and waveguide interface. Consequently, an undesired change in the optical transmission (up to 50%) can occur.[20,32] Note that for PCM-based photonic memories, controlled optical transmission change due to the absorption of light in the PCM is desired. The change in the transmission due to the scattering of light is considered uncontrolled transmission change and puts further limitations on PCM-based photonic memory design and performance. Hence, the optical transmission of the PCM cell should follow the trend of total optical absorption in the PCMs to minimize the effect of unwanted transmission change in the memory cell due to light scattering and back reflections. This means that for a PCM-based photonic memory cell, if the total amount of absorbed light in the PCM cell is n%, the optical transmission at the output of the cell should be $(100 - n)$%.

Lumerical FDTD was used to perform a comprehensive design-space exploration for the cell geometries in Fig. 4 with a fixed PCM length of 2 μm. Note that the 2-μm length of the PCM is enough to induce sufficient and observable transmission contrast to store the data and memory readout.[18,25] GST and GSST were used in these simulations. For each design point of PCM (waveguide) width and thickness, the transmission contrast ($\Delta T^{\text{opt}} = T_a^{\text{opt}} - T_c^{\text{opt}}$) between the crystalline and amorphous states and the total fraction of the power absorbed (P_{abs}) in the PCM when it is in the amorphous and crystalline state were recorded. Then, the transmission change stemming from scattering and back-reflections (ΔT_s^{opt}) was calculated using:

$$\Delta T_{s_{a/c}}^{\text{opt}} = T_{a/c}^{\text{opt}} - T_{s_{a/c}}^{\text{opt}}, \tag{6}$$

where

$$T_{s_{a/c}}^{\text{opt}} = 1 - P_{\text{abs}_{a/c}}. \tag{7}$$

Note that for an ideal transmission change due to phase change of the PCM, $T_{a/c}^{\text{opt}} - T_{s_{a/c}}^{\text{opt}} \approx 0$ meaning that transmission change is due to the absorption of the PCM. For example, when the PCM is in the amorphous state. $T_a^{\text{opt}} \approx 1$ is desirable meaning that the material absorption should be close to zero ($P_{\text{abs}} \approx 0$) and this leads to $T_{s_a}^{\text{opt}} \approx 1$. Consequently, $\Delta T_{s_a}^{\text{opt}} = T_a^{\text{opt}} - T_{s_a}^{\text{opt}} \approx 0$. A similar conclusion can be made when the PCM is in the crystalline state. The results for ΔT_s^{opt} and ΔT^{opt} when silicon nitride is used as the waveguide material (see Figs. 4(a) and 4(b)) are reported in Fig. 6. Observe that the maximum achievable absorption-induced transmission change in silicon nitride waveguides is 91% and 80% when GST and GSST integrated to a silicon nitride strip waveguide, respectively. In addition, the PCM thickness plays a vital role in inducing the scattering of light. Considering ΔT_s^{opt} values <10% and a minimum 6% margin between distinctive transmission levels,[4] silicon nitride waveguides can store up to 4-bits per cell when the optimum geometries were used for the waveguide and PCM cell. As for the PCM-based memory cells based on silicon nitride ridge waveguide, the results for ΔT_s^{opt} and ΔT^{opt} are reported in Fig. 7. Observe that when the ridge waveguide is used, the ΔT^{opt} is significantly lower compared to the strip waveguide design (60% for GST and 69% for GSST), meaning that the cell can store up to 3 bits.

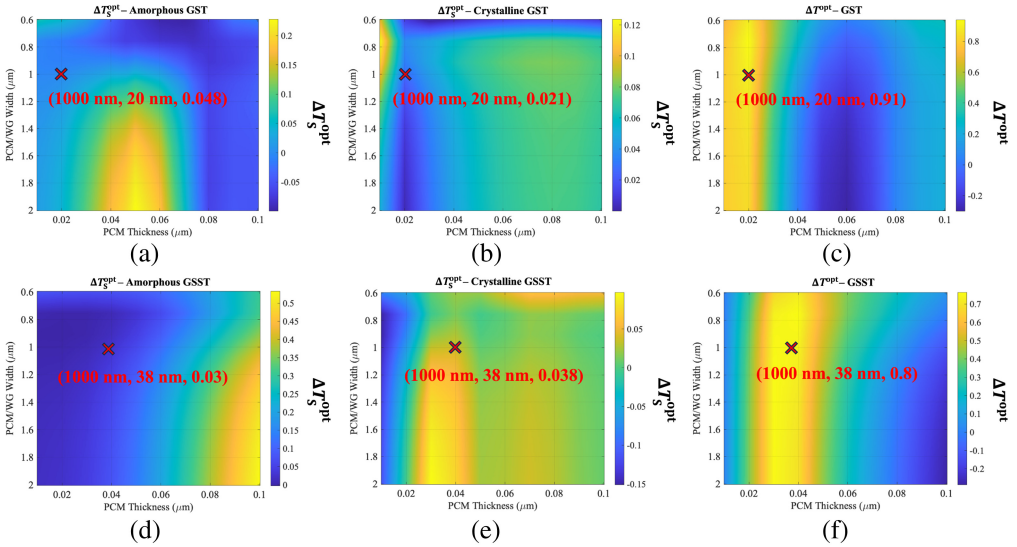

Fig. 6 Design-space exploration of PCM-based photonic memory cells based on silicon nitride strip waveguide with a thickness of 600 nm to study the optical loss due to scattering and back-reflection of the light to maximize the bit-density of the cell. The width of the waveguide and the PCM have been considered the same for all of the design points. ΔT_s^{opt} and ΔT^{opt} are reported based on the fraction of the input power for crystalline and amorphous states. (a)–(c) ΔT_s^{opt} and ΔT^{opt} for crystalline and amorphous GST, (d)–(f) ΔT_s^{opt} and ΔT^{opt} for crystalline and amorphous GSST ($\Delta T^{\text{opt}} = T_a^{\text{opt}} - T_c^{\text{opt}}$ and $\Delta T_{s_{a/c}}^{\text{opt}} = T_{a/c}^{\text{opt}} - T_{s_{a/c}}^{\text{opt}}$).

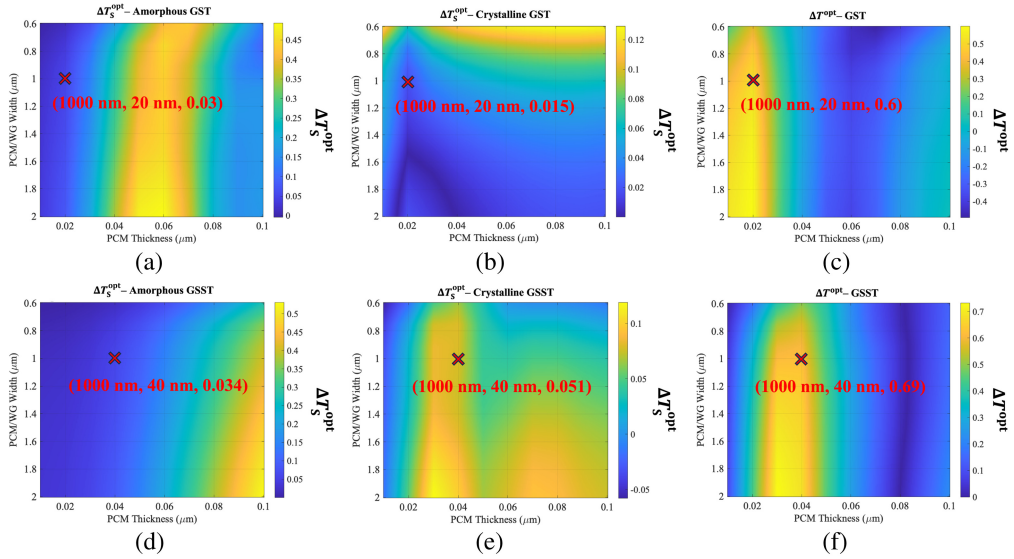

Fig. 7 Design-space exploration of PCM-based photonic memory cells based on silicon nitride ridge waveguide with a thickness of 600 nm and slab thickness of 360 nm to study the optical loss due to scattering and back-reflection of the light to maximize the bit-density of the cell. The width of the waveguide and the PCM has been considered the same for all design space points. ΔT_s^{opt} and ΔT^{opt} are reported based on the fraction of the input power for crystalline and amorphous state. (a)–(c) ΔT_s^{opt} and ΔT^{opt} for crystalline and amorphous GST, (d)–(f) ΔT_s^{opt} and ΔT^{opt} for crystalline and amorphous GSST ($\Delta T^{\text{opt}} = T_a^{\text{opt}} - T_c^{\text{opt}}$ and $\Delta T_{s_{a/c}}^{\text{opt}} = T_{a/c}^{\text{opt}} - T_{s_{a/c}}^{\text{opt}}$).

We performed the same analyses when the waveguide material was considered to be silicon. The results for ΔT_s^{opt} and ΔT^{opt} are reported in Figs. 8 and 9. Note that the refractive index contrast between the silicon and PCMs is lower, hence the optical mode is more confined in the waveguide. This leads to a more gradual interaction between PCM and the waveguide, hence the light will be less scattered. We can see from Fig. 8 that PCM-based photonic memories based on silicon strip waveguide can store up to 4 bit per cell when GST is used, which leads to 16 distinctive optical transmission levels considering 6% margin among transmission levels and ΔT_s^{opt} values <10%, which is higher compared to the case where GSST is used with the ability to store up to 3bits per cell. As for the case where a silicon ridge waveguide is used (see Fig. 9), we can see that the cells based on both GST and GSST can store up to 4 bits, satisfying the requirements for ΔT_s^{opt} and the margin among the transmission levels. Note that silicon offers a more compact footprint compared to silicon nitride to implement PCM-based photonic memories.[27] Note that in all of the cases, the range for ΔT_s^{opt} is higher in the amorphous state compared to the crystalline state. The reason for this is that PCMs in the crystalline state are extremely more absorptive and the scattered and back-reflected light could still be absorbed in the PCM through the second and third absorption processes. Note that to validate the simulation results, a case study for silicon nitride ridge waveguide with the thickness of 330 nm and slab thickness of 165 nm with air cladding is simulated according to the design reported by Rios et al.[14] The PCM used for this design was a 10 nm thin layer of GST with a length of 5 μm. The simulation results showed 80% of total optical power absorption, which is in good agreement with the reported value of 80.7% in Ref. 14. Note that the results for design-space exploration of optical transmission (T_s^{opt} and T_a^{opt}) for PCM-based photonic memory cells using silicon and silicon nitride waveguides with strip and ridge design are reported in Appendix A, Figs. 14 and 15. Moreover, the 3D FDTD simulation of electric field profile for the optimal designs for PCM-based photonic memory cells reported in this section are depicted in Appendix B, Figs. 16 and 17.

3.3 Heater Design and Cooling Time

A heat source should be used to initiate the phase change in PCMs. The required energy for phase change in PCM-based reconfigurable photonic devices can be provided by high-power laser pulses, a p- or n-doped resistive silicon heater, or a metallic heater. Compared to metallic heaters,

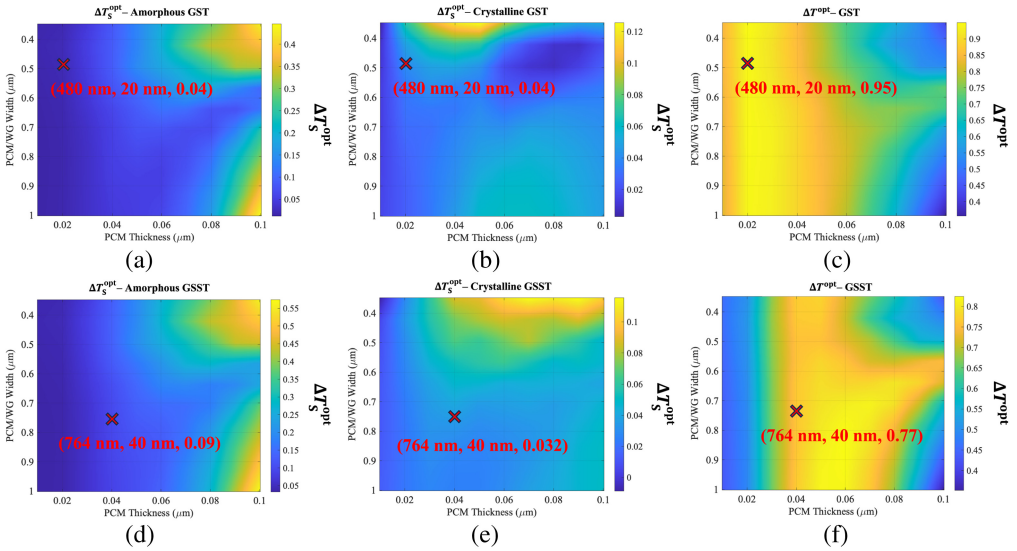

Fig. 8 Design-space exploration of PCM-based photonic memory cells based on silicon strip waveguide with a thickness of 220 nm to study the optical loss due to scattering and back-reflection of the light to maximize the bit-density of the cell. The width of the waveguide and the PCM has been considered the same for all design space points. ΔT_s^{opt} and ΔT^{opt} are reported based on the fraction of the input power for crystalline and amorphous states. (a)–(c) ΔT_s^{opt} and ΔT^{opt} for crystalline and amorphous GST, (d)–(f) ΔT_s^{opt} and ΔT^{opt} for crystalline and amorphous GSST ($\Delta T^{\text{opt}} = T_a^{\text{opt}} - T_c^{\text{opt}}$ and $\Delta T_{s_{a/c}}^{\text{opt}} = T_{a/c}^{\text{opt}} - T_{s_{a/c}}^{\text{opt}}$).

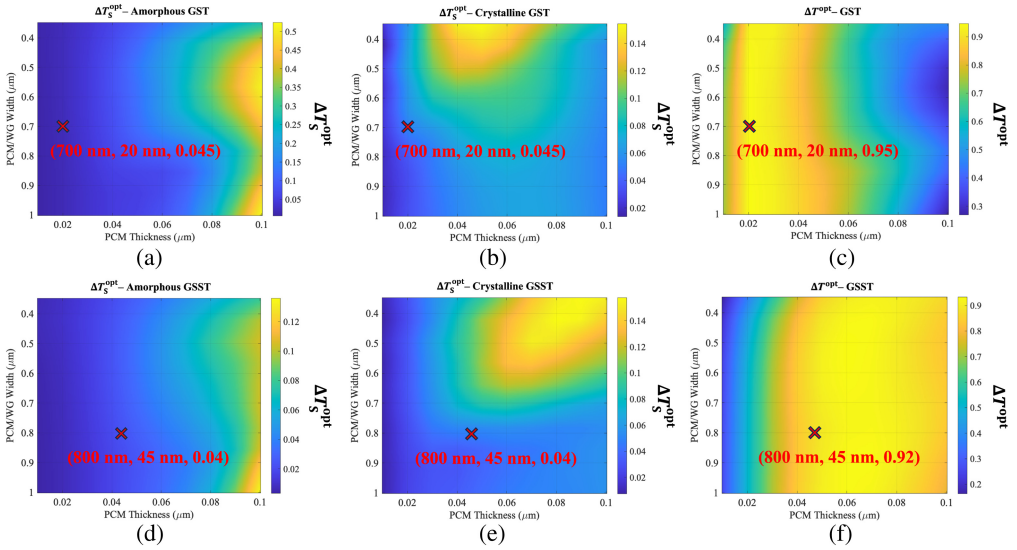

Fig. 9 Design-space exploration of PCM-based photonic memory cells based on silicon ridge waveguide with a thickness of 220 nm and slab thickness of 90 nm to study the optical loss due to scattering and back-reflection of the light to maximize the bit-density of the cell. The width of the waveguide and the PCM has been considered the same for all design space points. ΔT_s^{opt} and ΔT^{opt} are reported based on the fraction of the input power for crystalline and amorphous states. (a)–(c) ΔT_s^{opt} and ΔT^{opt} for crystalline and amorphous GST, (d)–(f) ΔT_s^{opt} and ΔT^{opt} for crystalline and amorphous GSST ($\Delta T^{\text{opt}} = T_a^{\text{opt}} - T_c^{\text{opt}}$ and $\Delta T_{s_{a/c}}^{\text{opt}} = T_{a/c}^{\text{opt}} - T_{s_{a/c}}^{\text{opt}}$).

resistive heaters based on p- or n-doped silicon may suffer from electromigration, especially for high-energy pulses, which limits the durability and stability of the heater to program the PCMs.[48] Moreover, resistive-based heaters may suffer from a large footprint (12.5 to 100 μm^2), excessive propagation loss due to the presence of the dopants in the silicon substrate,[17] and fundamental limitations in terms of the maximum power that can be provided by the resistive-based heaters.[31]

Although there are experimental works based on using p- or n-doped silicon as a heater for phase change of PCMs,[17,31,49] their endurance and thermal stability over time require further research.

Using laser pulses to write on the PCMs leads to efficient heating of the PCM with relatively low cooling time. However, an additional electro-optic and optical-electron conversion unit is required to drive the multiple laser sources and translate the electrical signal coming from the memory controller to the optical laser pulse and vice versa.[4] This will deteriorate the complexity and power overhead while limiting the speed of the whole memory system.[11,12,46,50,51]

In this paper, we opted to design a conventional Ti/TiN-based microheater proposed by CEA-leti due to its endurance and thermal stability over time to provide the required heat for triggering the phase change of PCMs. In the previous section, we showed that GST is the best option for implementing PCM-based photonic memory cells. This motivates the choice of GST as a case study in this section for designing an efficient microheater.

In this section, using multi-physics simulations, we discuss a design-space exploration to obtain an energy-efficient Ti/TiN-based microheater that can provide the required energy to trigger the phase change mechanism in the PCM. We started the design-space exploration by analyzing the optical loss of the cell due to the light absorption in the heater's material for the different designs presented in the previous section. The heater considered in this analysis is 70-nm thick with a width of at least 1 μm, required by CEA-leti. Note that the complex refractive index of the Ti/TiN heater is a function of temperature through the thermo-optic effect. The FDTD simulations showed that the optical loss due to absorption of light in the heater's material will change by <3%, even when the melting point of the heater is reached. The results of the optical transmission as a function of the width difference between the waveguide and the heater and the gap between the heater and waveguide are reported in Figs. 10 and 11. We can see that for gaps larger than 200 nm between the heater and the waveguide, the optical transmission is about 100%, meaning that the metal-light interaction, hence the metal absorption, is negligible for this configuration.

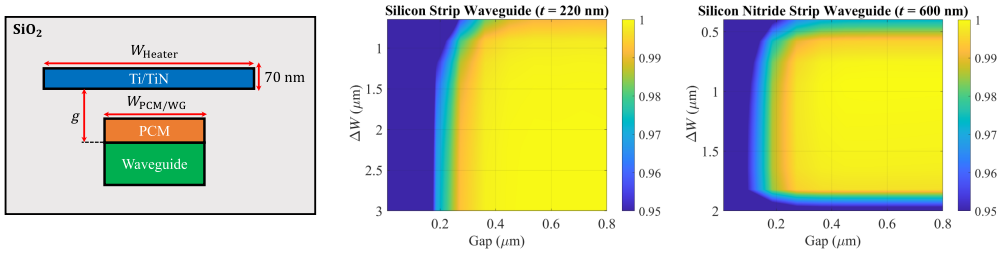

Fig. 10 Optical transmission of the cell in the presence of the TiN heater when strip design is used for the waveguide. (a) Schematic design of the metallic heater considered in this work, (b) the power transmission values for silicon strip waveguide with a thickness of 220 nm, and (c) the power transmission values for silicon nitride strip waveguide with the thickness of 600 nm. ($\Delta W = W_{PCM/WG} - W_{Heater}$).

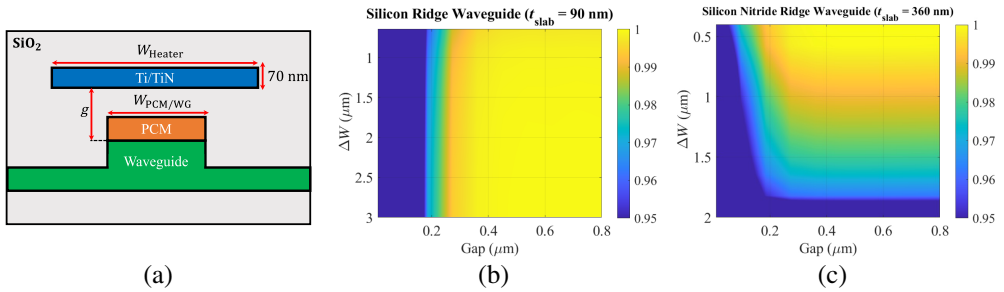

Fig. 11 Optical transmission of the cell in the presence of the TiN heater when ridge design is used for the waveguide. (a) Schematic design of the metallic heater considered in this work, (b) the power transmission values for silicon ridge waveguide with a thickness of 220 nm and slab thickness of 90 nm, and (c) the power transmission values for silicon nitride ridge waveguide with the thickness of 600 nm and slab thickness of 360 nm. ($\Delta W = W_{PCM/WG} - W_{Heater}$).

Starting from the minimum gap to have the lossless transmission, transient unsteady-state heat simulation was carried out to solve the heat transfer equation (see Fig. 2) using Lumerical HEAT solver with the parameters mentioned in Table 1 to capture the temperature profile evolution within the PCM as a function of time for different gaps between the waveguide and heater. This analysis aimed to find (1) the optimized gap for the heater in terms of the cooling of the PCM so it can be ready for the next cycle of read, set, or reset, and (2) the energy efficiency of the heater/PCM. To do this, heat pulses with different power values and duration were provided by the heater. Note that for all of the design points, the heat pulse has a relatively high power (up to 30 mW) and a short duration (<2 μs) to mimic the reset (amorphization) of the cell.[10,14,17,25] Three case studies for a heater based on Ti/TiN with a fixed width of 2 μm were considered for this analysis to generate uniform heat for the PCM. The first case study was the case where the gap between the heater and the waveguide was 200 nm; for the second case, the gap was considered to be 400 nm; and for the last case, a 600-nm gap was considered. For each case study, the example design of silicon strip waveguide with width and thickness of 480 and 220 nm, respectively, integrated with a 20 nm thick GST is considered and the pulse powers and their corresponding duration are chosen to ensure that the temperature within the PCM does not reach temperatures higher than melting temperatures. Note that the chosen example design for PCM-based photonic memory cell offers the single-mode propagation of the light, minimized transmission change due to scattering and back-reflections, maximum optical transmission contrast between amorphous and crystalline states with 20 nm thin GST layer. The temperature profile for this design for the three gap values of 200, 400, and 600 nm between the waveguide and the heater when the pulse power is 10 mW is reported in Fig. 12(a). Observe that as the gap between the waveguide and the heater increases, higher values of pulse duration that translate to higher energy values ($E = P.t$) must be used to melt the PCM. Note that because of the short duration of the reset heat pulse, the material cannot reach its thermal equilibrium; thus, increasing the heat pulse duration increases the temperature within the PCM. In addition, we can see that as the gap between the heater and the waveguide increases, the cooling of (discussed below) the PCM will be significantly slower. Note that for the set pulse where the crystallization of the PCM happens, the PCM is already in the stable state and the only requirement is having a low power pulse for a significantly long duration to have a complete crystallization.[20]

To analyze the cooling time of the GST cell considered in Fig. 12(a) for different gaps between the heater and the waveguide, the time that it takes for the PCM to reach the glass temperature when the heat source is turned off is considered (see Fig. 12(a)). The results for the cooling time for different values of the gap, pulse power, and its corresponding duration and temperature are reported in Figs. 12(b) and 12(c). Observe that, as expected, as the gap between the heater and waveguide increases from 200 to 600 nm, the maximum cooling time significantly increases from 3.4 to 7.5 μs, meaning that the lower gap values result in higher energy efficiency of the cell. This is due to the fact that for higher gaps, when the heat source is turned off, due to the larger distance between the heater and the PCM, it will take longer for the heat energy to be exchanged between the source, oxide layer, and the PCM until it is dissipated and reach the room temperature.

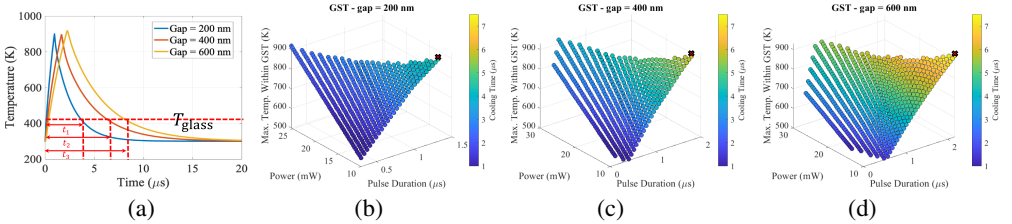

Fig. 12 Transient unsteady state heat simulation results. (a) Temperature evolution in time, when the pulse power is 10 mW, $t_{1,2,3}$, is the required cool time for PCM so it can be ready for the next programming cycle. (b) Design-space exploration using pulse power, pulse duration, and cooling time for a 20-nm thick GST cell and 200 nm gap between the heater and the waveguide. (c) Design-space exploration using pulse power, pulse duration, and cooling time for a 20-nm GST cell and 400 nm gap between the heater and the waveguide. (d) Design-space exploration using pulse power, pulse duration, and cooling time for a 20-nm GST cell and 200 nm gap between the heater and the waveguide.

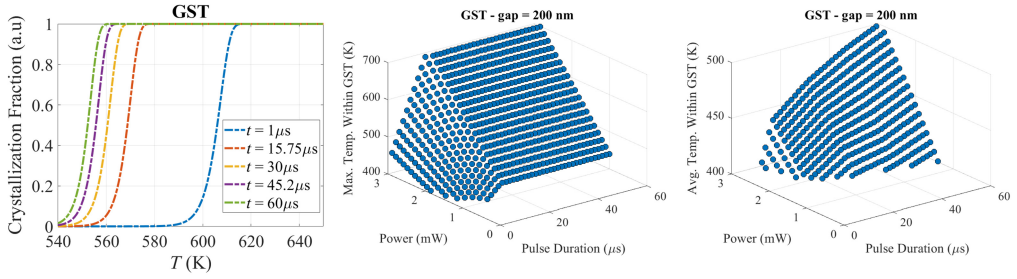

Fig. 13 (a) Crystallization fraction at different isothermal temperatures for different values of heat duration, calculated using Eqs. (3) and (4). (b) Design-space exploration of the maximum temperature within the GST for different heat power and duration values. (c) Design-space exploration of the average temperature within the GST for different heat power and duration values.

Moreover, observe that for a fixed gap between the heater and the waveguide, increasing the temperature within the PCM leads to significantly higher cooling time. This makes the amorphization of the PCMs a more critical operation compared to crystallization as the PCM requires much higher energies to reach the melting point. Note that because of using a wide heater with uniform heat generation ($W_{\text{Heater}} = 2\ \mu$m), the required energy for GSST to melt will be slightly higher than GST as the melting temperature of the GSST is 900 K, and the cooling time will be even slower than the GST as the glass temperature of GSST is lower than GST (around 423 K[29]), which means it will take longer to reach this temperature.

We analyzed the crystallization kinetics of the GST-based photonic memory case study in this work based on Eqs. (3) and (4). As mentioned, in Eq. (4), E_a stands for the PCM's crystallization activation energy, which is 2.2 ev for GST;[33,35,36] ν stands for PCM's frequency factor, which is 1.79×10^{-24} s^{-1} for GST;[33] K_b is the Boltzmann constant; and T is the temperature of the PCM. The results for the crystallization fraction of GST as a function of its temperature after a variable isothermal pulse duration of t are depicted in Fig. 13(a). We can see that as the pulse duration decreases, the crystallization of the GST starts at higher temperatures meaning that the heat power should increase.[21] As the pulse duration increases, the crystallization starts at lower temperatures.

Note that doping the GST with nitrogen atoms leads to lower Avrami constant values compared to intrinsic GST, which results in a more gradual crystallization. Therefore, a higher number of stable crystallization levels in the presence of temperature variations can be achieved, which is consistent with the reported results in Ref. 25.

Observe from Fig. 13(a) that the crystallization of GST occurs with a sharp trend as a function of the temperature. This makes GST extremely susceptible to temperature variation of the heater and transmission drift. For a Ti/TiN-based heater with a gap of 200 nm from a silicon strip waveguide integrated with a 20-nm thick GST with a width of 480 nm, a design-space exploration for heating the PCM is performed to capture the maximum temperature within the PCM as a function of relatively lower heat pulse power values (up to 3 mW) and relatively longer pulse durations (up to 60 μs), compared to what is reported in Fig. 12. The results for the maximum temperature within the GST as a function of heat power and pulse duration are reported in Fig. 13(b). Note that the temperature in GST for the pulse durations longer than 16 μs becomes isothermal as the rate of heat transfer from the PCM to silicon waveguide and oxide cladding also increases due to thermal conduction, meaning that further increase in the pulse duration will not increase the temperature within the PCM unless the heat power increases. Moreover, observe from Fig. 13(a) that as the pulse duration decreases, to trigger the crystallization of GST, the heat source must maintain the temperature of GST at higher temperatures to start the crystallization. The results presented in this section show the essential need for a multi-step programming scheme to maintain the temperature for a specific duration to benefit from the low-latency crystallization of PCMs.

4 Conclusion

In this article, we have described a comprehensive material-level and device-level design-space exploration and performance comparison of PCM-based photonic memory cells using two well-known PCMs of GST and GSST, integrated with silicon and silicon nitride waveguides.

We showed that using silicon waveguides integrated with PCMs can lead to a more reliable solution with lower optical scattering and higher bit densities per cells, compared to silicon nitride waveguides. Moreover, we showed that when a metallic microheater is used to heat the PCM, as the gap between the waveguide and the metallic plate decreases, the cell will be more efficient and have a lower cooling time. The results and outcomes presented in this paper provide valuable insights for photonic system engineers to design PCM-based photonic memory arrays for main memory and in-memory photonic computing units.

5 Appendix A: Optical Transmission of PCM-Based Photonic Memory Cells

The design-space exploration of optical transmission spectrum for PCM in amorphous and crystalline states when integrated on top of silicon and silicon nitride waveguide with strip and ridge design is reported in Figs. 14 and 15. Observe that compared to silicon waveguides, using silicon nitride waveguide leads to higher unwanted optical transmission change due to scattering of the light hence lower optical transmission contrast to store the data.

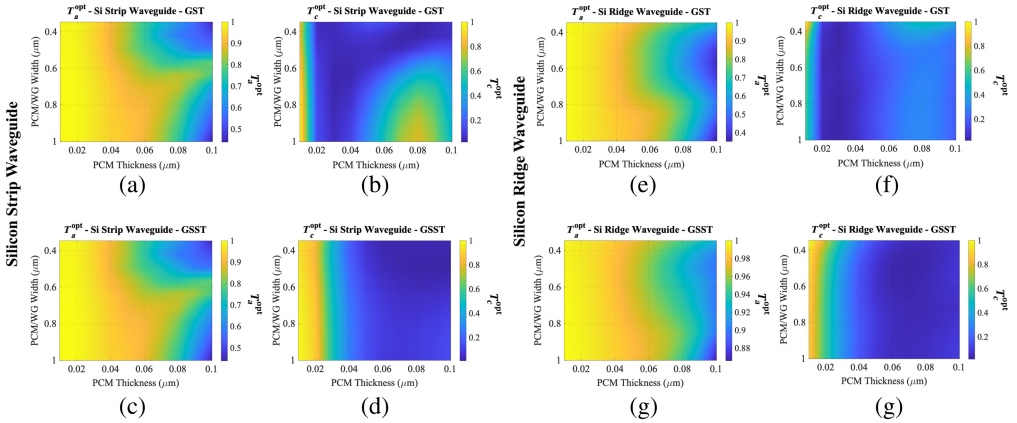

Fig. 14 Design-space exploration of PCM-based photonic memory cells based on silicon strip and ridge waveguide with a thickness of 220 nm to study the optical transmission of the cell for different design points (see Fig. 4). The width of the waveguide and the PCM has been considered the same for all design space points. T^{opt} reported based on the fraction of the input power for crystalline and amorphous. (a)–(d) $T^{\text{opt}}_{a/c}$ for GST and GSST-based cells when silicon strip waveguide is used, (e)–(h) $T^{\text{opt}}_{a/c}$ for GST and GSST-based cells when silicon ridge waveguide is used.

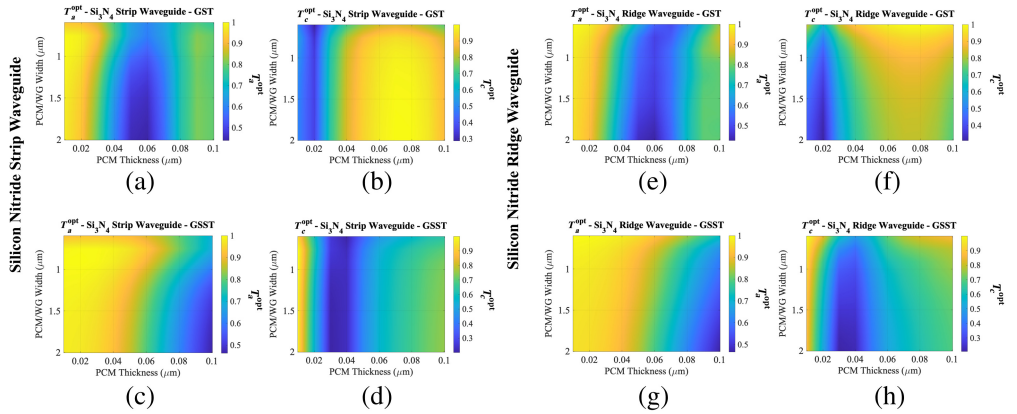

Fig. 15 Design-space exploration of PCM-based photonic memory cells based on silicon nitride strip and ridge waveguide with a thickness of 600 nm to study the optical transmission of the cell for different design points (see Fig. 4). The width of the waveguide and the PCM has been considered the same for all design space points. T^{opt} reported based on the fraction of the input power for crystalline and amorphous. (a)–(d) $T^{\text{opt}}_{a/c}$ for GST and GSST-based cells when silicon nitride strip waveguide is used. (e)–(h) $T^{\text{opt}}_{a/c}$ for GST and GSST-based cells when silicon nitride ridge waveguide is used.

6 Appendix B: Electric Field Profile of the Optimized Designs for PCM-Based Photonic Memory Cells

The electric field profile for fundamental TE mode (Ey) and its interaction with PCM when the optimal designs for PCM/waveguide is used according to 2.3. Observe that using silicon nitride waveguide leads to scattering a higher portion of the propagating electric field when interacting with PCM due to weaker mode confinement compared to silicon waveguide (Figs. 16 and 17).

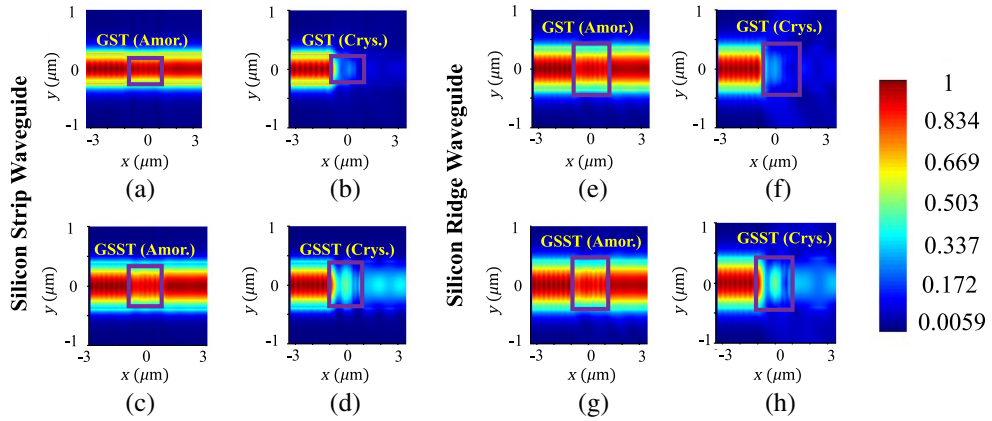

Fig. 16 Simulated electric field in the XY cut plane (Z-axis is aligned with the thickness of PCM/Waveguide) for the optimized geometry marked in Figs. 8 and 9. (a)–(d) Electric field distribution for the optimized designs for GST ($W = 480$ nm and $t = 20$ nm) and GSST-based cells ($W = 764$ nm and $t = 40$ nm) when silicon strip waveguide is used. (e)–(h) Electric field distribution for the optimized designs for GST ($W = 700$ nm and $t = 20$ nm) and GSST-based cells ($W = 800$ nm and $t = 45$ nm) when silicon ridge waveguide is used. The purple box in the figures denotes the location of PCM on top of the waveguide.

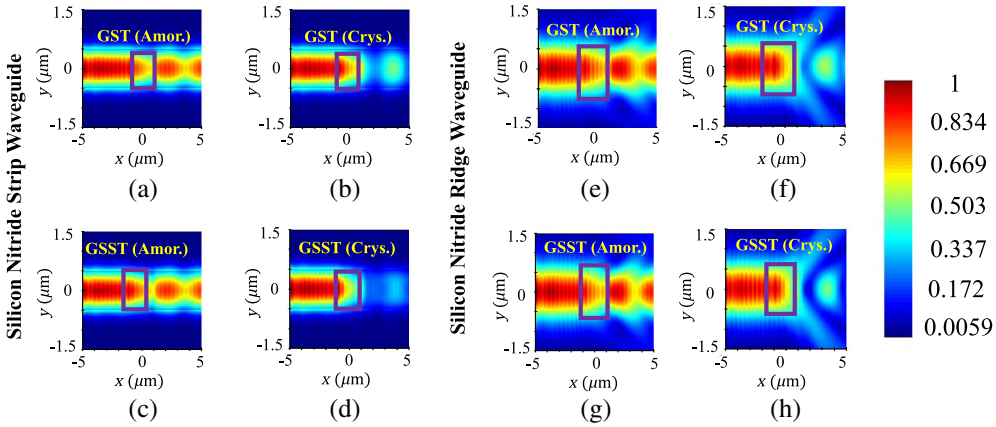

Fig. 17 Simulated electric field in the XY cut plane (Z-axis is aligned with the thickness of PCM/Waveguide) for the optimized geometry marked in Figs. 6 and 7. (a)–(d) Electric field distribution for the optimized designs for GST ($W = 1000$ nm and $t = 20$ nm) and GSST-based cells ($W = 1000$ nm and $t = 38$ nm) when silicon nitride strip waveguide is used. (e)–(h) Electric field distribution for the optimized designs for GST ($W = 1000$ nm and $t = 20$ nm) and GSST-based cells ($W = 1000$ nm and $t = 40$ nm) when silicon nitride ridge waveguide is used. The purple box in the figures denotes the location of PCM on top of the waveguide.

Code and Data Availability

The data that support the findings of this study are available from the corresponding author, Mahdi Nikdast, upon reasonable request.

Acknowledgments

This work was supported in part by the National Science Foundation (NSF) (Grant Nos. CCF-2006788 and CNS-2046226).

References

1. I. G. Thakkar and S. Pasricha, "DyPhase: a dynamic phase change memory architecture with symmetric write latency and restorable endurance," *IEEE Trans. Comput.-Aid. Des. Integrated Circuits Syst.* **37**(9), 1760–1773 (2017).
2. M. Mohseni and A. H. Novin, "A survey on techniques for improving phase change memory (PCM) lifetime," *J. Syst. Archit.* **144**, 103008 (2023).
3. B. Jahannia, S. A. Ghasemi, and H. Farbeh, "Multi-retention STT-MRAM architectures for IoT: evaluating the impact of retention levels and memory mapping schemes," *IEEE Access* **12**, 26562–26580 (2024).
4. F. Sunny et al., "Comet: a cross-layer optimized optical phase-change main memory architecture," in *Des., Autom. & Test in Eur. Conf. & Exhibit. (DATE)*, IEEE, pp. 1–6 (2024).
5. J. Boukhobza et al., "Emerging NVM: a survey on architectural integration and research challenges," *ACM Trans. Des. Autom. Electron. Syst.* **23**(2), 1–32 (2017).
6. O. Mutlu, "Memory scaling: a systems architecture perspective," in *5th IEEE Int. Memory Workshop*, IEEE, pp. 21–25 (2013).
7. Y. Chen, "ReRAM: history, status, and future," *IEEE Trans. Electron Devices* **67**(4), 1420–1433 (2020).
8. M. Mohseni and A. H. Novin, "OML-PCM: optical multi-level phase change memory architecture for embedded computing systems," *Eng. Res. Express* **5**(4), 045078 (2023).
9. K. Aryana et al., "Optical and thermal properties of Ge_2 Sb_2 Te_5, Sb_2Se_3, and Sb_2S_3 for reconfigurable photonic devices," *Opt. Mater. Express* **13**(11), 3277–3286 (2023).
10. X. Li et al., "Fast and reliable storage using a 5 bit, nonvolatile photonic memory cell," *Optica* **6**(1), 1–6 (2019).
11. A. Shafiee, S. Pasricha, and M. Nikdast, "A survey on optical phase-change memory: the promise and challenges," *IEEE Access* **11**, 11781–11803 (2023).
12. A. Shafiee et al., "Compact and low-loss PCM-based silicon photonic MZIs for photonic neural networks," in *IEEE Photonics Conf. (IPC)*, IEEE, pp. 1–2 (2023).
13. G. W. Burr et al., "Phase change memory technology," *J. Vac. Sci. Technol. B* **28**(2), 223–262 (2010).
14. C. Ríos et al., "Integrated all-photonic non-volatile multi-level memory," *Nat. Photonics* **9**(11), 725–732 (2015).
15. Z. Fang et al., "Non-volatile reconfigurable silicon photonics based on phase-change materials," *IEEE J. Sel. Top. Quantum Electron.* **28**(3), 1–17 (2021).
16. A. Shafiee et al., "Design space exploration for PCM-based photonic memory," in *Proc. Great Lakes Symp. on VLSI*, pp. 533–538 (2023).
17. C. Ríos et al., "Ultra-compact nonvolatile phase shifter based on electrically reprogrammable transparent phase change materials," *PhotoniX* **3**(1), 26 (2022).
18. J. Feldmann et al., "Integrated 256 cell photonic phase-change memory with 512-bit capacity," *IEEE J. Sel. Top. Quantum Electron.* **26**(2), 8301807 (2019).
19. M. Wuttig, H. Bhaskaran, and T. Taubner, "Phase-change materials for non-volatile photonic applications," *Nat. Photonics* **11**(8), 465–476 (2017).
20. C. A. R. Ocampo et al., "New phase-change materials for photonic computing and beyond," in *Phase Change Materials-Based Photonic Computing*, H. Bhaskaran and W. H. P. Pernice, Eds., pp. 145–192, Elsevier (2024).
21. Y. Wang et al., "A scheme for simulating multi-level phase change photonics materials," *NPJ Comput. Mater.* **7**(1), 183 (2021).
22. W. H. Pernice and H. Bhaskaran, "Introduction to phase change photonics," in *Phase Change Materials-Based Photonic Computing*, H. Bhaskaran and W. H. P. Pernice, Eds., pp. 1–10, Elsevier (2024).
23. Y.-S. Huang et al., "Tunable structural transmissive color in fano-resonant optical coatings employing phase-change materials," arXiv:2302.03207 (2023).
24. T. Y. Teo et al., "Comparison and analysis of phase change materials-based reconfigurable silicon photonic directional couplers," *Opt. Mater. Express* **12**(2), 606–621 (2022).
25. J. Xia et al., "Seven bit nonvolatile electrically programmable photonics based on phase-change materials for image recognition," *ACS Photonics* **11**(2), 723–730 (2024).
26. C. Ros et al., "In-memory computing on a photonic platform," *Sci. Adv.* **5**(2), eaau5759 (2019).
27. X. Li et al., "Experimental investigation of silicon and silicon nitride platforms for phase-change photonic in-memory computing," *Optica* **7**(3), 218–225 (2020).
28. N. Youngblood et al., "Tunable volatility of $Ge_2Sb_2Te_5$ in integrated photonics," *Adv. Funct. Mater.* **29**(11), 1807571 (2019).

29. K. Aryana et al., "Suppressed electronic contribution in thermal conductivity of $Ge_2Sb_2Se_4Te$," *Nat. Commun.* **12**(1), 7187 (2021).
30. J. Gosciniak, "Waveguide-integrated plasmonic photodetectors and activation function units with phase change materials," *IEEE Photonics J.* **16**(1), 4800110 (2023).
31. J. R. Erickson et al., "Comparing the thermal performance and endurance of resistive and pin silicon microheaters for phase-change photonic applications," *Opt. Mater. Express* **13**(6), 1677–1688 (2023).
32. J. Li et al., "Performance limits of phase change integrated photonics," *IEEE J. Sel. Top. Quantum Electron.* **30**(4), 6100109 (2024).
33. I. Yang et al., "Effect of doped nitrogen on the crystallization behaviors of $Ge_2Sb_2Te_5$," *J. Electrochem. Soc.* **157**(4), H483 (2010).
34. B. Chen et al., "Crystallization kinetics of GeSbTe phase-change nanoparticles resolved by ultrafast calorimetry," *J. Phys. Chem. C* **121**(15), 8569–8578 (2017).
35. S. Senkader and C. Wright, "Models for phase-change of $Ge_2Sb_2Te_5$ in optical and electrical memory devices," *J. Appl. Phys.* **95**(2), 504–511 (2004).
36. J. A. Frantz et al., "Optical constants of germanium antimony telluride (GST) in amorphous, crystalline, and intermediate states," *Opt. Mater. Express* **13**(12), 3631–3640 (2023).
37. A. Shafiee et al., "A multiphysics simulation approach for photonic devices integrating phase change materials," in *Int. Conf. Numer. Simul. of Optoelectron. Devices (NUSOD)*, IEEE, pp. 119–120 (2023).
38. A. Sebastian et al., "Memory devices and applications for in-memory computing," *Nat. Nanotechnol.* **15**(7), 529–544 (2020).
39. C. Rios et al., "Controlled switching of phase-change materials by evanescent-field coupling in integrated photonics," *Opt. Mater. Express* **8**(9), 2455–2470 (2018).
40. I. Khan et al., "Optimized management of ultra-wideband photonics switching systems assisted by machine learning," *Opt. Express* **30**(3), 3989–4004 (2022).
41. L. Tunesi et al., "Design and performance assessment of modular multi-band photonic-integrated WSS," *Opt. Express* **31**(22), 36486–36502 (2023).
42. Z. Ghanaatian, A. Shafiee, and M. Nikdast, "Variation-aware layout and design optimization of silicon photonic Mach–Zehnder interferometers," in *IEEE Photonics Conf. (IPC)*, IEEE, pp. 1–2 (2023).
43. C. Li et al., "Understanding phase-change materials with unexpectedly low resistance drift for phase-change memories," *J. Mater. Chem. C* **6**(13), 3387–3394 (2018).
44. J. Y. Raty et al., "Aging mechanisms in amorphous phase-change materials," *Nat. Commun.* **6**(1), 7467 (2015).
45. J. Meng et al., "Electrical programmable multilevel nonvolatile photonic random-access memory," *Light: Sci. Appl.* **12**(1), 189 (2023).
46. A. Narayan et al., "Architecting optically controlled phase change memory," *ACM Trans. Archit. Code Optim.* **19**(4), 1–26 (2022).
47. K. Aryana et al., "Toward accurate thermal modeling of phase change material-based photonic devices," *Small* **19**(50), 2304145 (2023).
48. J. Lloyd, M. Polcari, and G. MacKenzie, "Observation of electromigration in heavily doped polycrystalline silicon thin films," *Appl. Phys. Lett.* **36**(6), 428–430 (1980).
49. Z. Fang et al., "Arbitrary programming of racetrack resonators using low-loss phase-change material Sb_2Se_3," *Nano Lett.* **24**(1), 97–103 (2023).
50. N. Youngblood et al., "Realization of an integrated photonic platform for coherent photo-electric processing," *Opt. Open* (2023).
51. G. Yang et al., "Processing-in-memory using optically-addressed phase change memory," in *IEEE/ACM Int. Symp. Low Power Electron. and Des. (ISLPED)*, IEEE, pp. 1–6 (2023).

Amin Shafiee received his BSc degree in electronics engineering from Shiraz University, Iran, in 2018, and his MSc degree in integrated electronics and optoelectronics from Polytechnique University of Turin (Politecnico di Torino), Italy, in 2021. His research interests include silicon photonics for high-performance computation and communication, reconfigurable photonic devices, and photodetectors. He is a graduate research assistant at Colorado State University (CSU).

Benoit Charbonnier received his engineering degree in 1994 from Ecole Nationale Supérieure des Télécommunications de Paris and his PhD in 1997 on 40 Gbps soliton transmission from the same institution. He joined Nortel Network in 1997, working on 80 Gbps long haul transmission, then Marconi Communications in 2001, focusing on Ultra-Long Haul 10 Gb/s transmission products. In 2004, he joined Orange Labs as a research engineer, concentrating on next-gen optical access networks and digital signal processing in optical communications. Since 2015, he has led the photonics program at CEA-Leti, Grenoble, focusing on silicon photonics technologies and now oversees neuromorphic photonics applications in the silicon photonics lab.

Jie Yao received his PhD from UC Berkeley in 2010 and conducted postdoctoral research at Stanford University. Joining UC Berkeley's Materials Science and Engineering Department in 2013, his research centers on optical materials for nanophotonic applications, such as sensors and communication devices. He is developing new material platforms for low-power optoelectronic devices crucial for sustainable infrastructures and biomedical applications. He received the CAREER award from NSF, Early Career award from SPIE, Hellman Fellowship, and Bakar Fellowship from UC Berkeley.

Sudeep Pasricha received his BE degree in electronics and communications from Delhi Institute of Technology, India, and his MS and PhD degrees in computer science from the University of California, Irvine. He is currently a professor and chair of computer engineering at CSU, also holding positions in computer science and systems engineering. His research focuses on innovative software algorithms, hardware architectures, and hardware-software co-design for energy-efficient, fault-tolerant, real-time, and secure computing, emphasizing chip-scale photonic computation and communication.

Mahdi Nikdast is an associate professor and Endowed Rockwell-Anderson professor in the Department of Electrical and Computer Engineering at CSU in Fort Collins, Colorado, USA. He received his PhD in electronic and computer engineering from the Hong Kong University of Science and Technology in 2014. From 2014 to 2017, he served as a postdoctoral fellow at McGill University and Polytechnique Montreal, Canada. He directs the Electronic-PhotoniC System Design Laboratory at CSU, focusing on integrated photonics-based systems-on-chip and next-gen data-communication, computing, and sensing systems with an emphasis on energy efficiency and robustness. He and his students have received multiple best paper awards for their work in integrated photonics and design for manufacturability.